Thermal conductivity of rutile germanium dioxide

Cite as: Appl. Phys. Lett. 117, 102106 (2020); https://doi.org/10.1063/5.0011358 Submitted: 20 April 2020 . Accepted: 15 July 2020 . Published Online: 10 September 2020

S. Chae, 🗓 K. A. Mengle, R. Lu, A. Olvera, N. Sanders, J. Lee, 🗓 P. F. P. Poudeu, 🗓 J. T. Heron, and 🗓 E. Kioupakis

COLLECTIONS

Paper published as part of the special topic on Ultrawide Bandgap Semiconductors







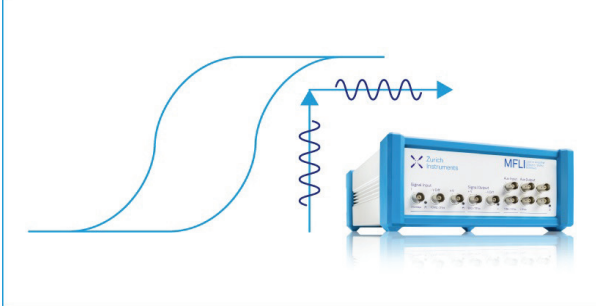
ARTICLES YOU MAY BE INTERESTED IN

Epitaxial stabilization of rutile germanium oxide thin film by molecular beam epitaxy Applied Physics Letters 117, 072105 (2020); https://doi.org/10.1063/5.0018031

Electron and hole mobility of rutile GeO₂ from first principles: An ultrawide-bandgap semiconductor for power electronics

Applied Physics Letters 117, 182104 (2020); https://doi.org/10.1063/5.0033284

Rutile GeO₂: An ultrawide-band-gap semiconductor with ambipolar doping Applied Physics Letters 114, 102104 (2019); https://doi.org/10.1063/1.5088370



Webinar How to Characterize Magnetic Materials Using Lock-in Amplifiers





Register now



Thermal conductivity of rutile germanium dioxide

Cite as: Appl. Phys. Lett. 117, 102106 (2020); doi: 10.1063/5.0011358 Submitted: 20 April 2020 · Accepted: 15 July 2020 · Published Online: 10 September 2020







S. Chae, K. A. Mengle, 🕞 R. Lu, A. Olvera, N. Sanders, J. Lee, P. F. P. Poudeu, 🕞 J. T. Heron, and E. Kioupakis and E. Kiou



AFFILIATIONS

Department of Materials Science and Engineering, University of Michigan, Ann Arbor, Michigan 48109, USA

Note: This paper is part of the Special Topic on Ultrawide Bandgap Semiconductors.

^{a)}Authors to whom correspondence should be addressed: jtheron@umich.edu and kioup@umich.edu

ABSTRACT

Power electronics seek to improve power conversion of devices by utilizing materials with a wide bandgap, high carrier mobility, and high thermal conductivity. Due to its wide bandgap of $4.5 \, \text{eV}$, β -Ga₂O₃ has received much attention for high-voltage electronic device research. However, it suffers from inefficient thermal conduction that originates from its low-symmetry crystal structure. Rutile germanium oxide (r-GeO₂) has been identified as an alternative ultra-wide-bandgap (4.68 eV) semiconductor with a predicted high electron mobility and ambipolar dopability; however, its thermal conductivity is unknown. Here, we characterize the thermal conductivity of r-GeO2 as a function of temperature by first-principles calculations, experimental synthesis, and thermal characterization. The calculations predict an anisotropic phonon-limited thermal conductivity for r-GeO₂ of 37 W m⁻¹ K⁻¹ along the a direction and 58 W m⁻¹ K⁻¹ along the c direction at 300 K where the phonon-limited thermal conductivity predominantly occurs via the acoustic modes. Experimentally, we measured a value of 51 W m⁻¹ K⁻¹ at 300 K for hot-pressed, polycrystalline r-GeO₂ pellets. The measured value is close to our directionally averaged theoretical value, and the temperature dependence of ~1/T is also consistent with our theory prediction, indicating that thermal transport in our r-GeO₂ samples at room temperature and above is governed by phonon scattering. Our results reveal that high-symmetry UWBG materials, such as r-GeO₂, may be the key to efficient power electronics.

Published under license by AIP Publishing. https://doi.org/10.1063/5.0011358

As the critical dielectric breakdown field of materials increases non-linearly with the increasing bandgap, ultra-wide bandgap (UWBG) semiconductors with gaps wider than GaN (3.4 eV) have emerged as compelling materials for high-power electronic applications. In addition to their wide bandgap, other desirable material properties for power electronics include the possibility of both n-type and p-type doping, high carrier mobilities to reduce energy lost during device operation, and high thermal conductivity to efficiently remove the generated waste heat.

Numerous UWBG semiconductors have been explored for power electronics; however, many of them face significant challenges in efficient thermal management. For example, β -Ga₂O₃ is one of the most popular UWBG materials, but its poor intrinsic thermal conductivity κ (11 W m⁻¹ K⁻¹ and 27 W m⁻¹ K⁻¹ along the \vec{a} and \vec{b} directions, respectively)^{2,3} is a crucial drawback. Other state-of-the-art UWBG materials, such as AlGaN/AlN and diamond, exhibit high intrinsic thermal conductivities. However, AlGaN/AlN is typically grown epitaxially on sapphire substrates with low thermal conductivity (34.6 W m⁻¹ K⁻¹), whereas the high cost of single-crystal AlN and diamond substrates that conduct heat efficiently poses an obstacle for adoption in devices.

Recently, first-principles calculations identified rutile GeO2 (r-GeO₂) as a promising but unexplored UWBG material for applications in high-power electronics. Its ultra-wide bandgap, experimentally measured at 4.68 eV⁴ and theoretically evaluated at 4.44–4.68 eV,^{5,6} is similar to that of β -Ga₂O₃. Moreover, whereas β -Ga₂O₃ can only be doped n-type, r-GeO₂ has promising doping properties with shallow ionization energies for donors and an ionization energy of 0.45 eV for Al acceptors. In addition, we recently evaluated its intrinsic phononlimited electron mobility and dielectric breakdown and predicted its Baliga Figure of Merit (BFOM) to be higher than that of β -Ga₂O₃. Unlike the monoclinic crystal structure of β -Ga₂O₃, r-GeO₂ has a more symmetric tetragonal crystal structure with fewer atoms in the unit cell [Fig. 1(a)]. Thus, we expect that the intrinsic phonon-limited thermal conductivity of r-GeO₂ is higher than that of β -Ga₂O₃ due to reduced phonon-band folding. Moreover, we anticipate that r-GeO₂ can be grown on thermally conductive rutile substrates such as SnO₂ $(\kappa \sim 100 \,\mathrm{W m^{-1} K^{-1}})$. However, the thermal conductivity of r-GeO₂ has not previously been reported.

In this work, we investigate the thermal conductivity of r-GeO₂ by both first-principles calculations and experimental measurements on polycrystalline samples. Our calculations show that the intrinsic

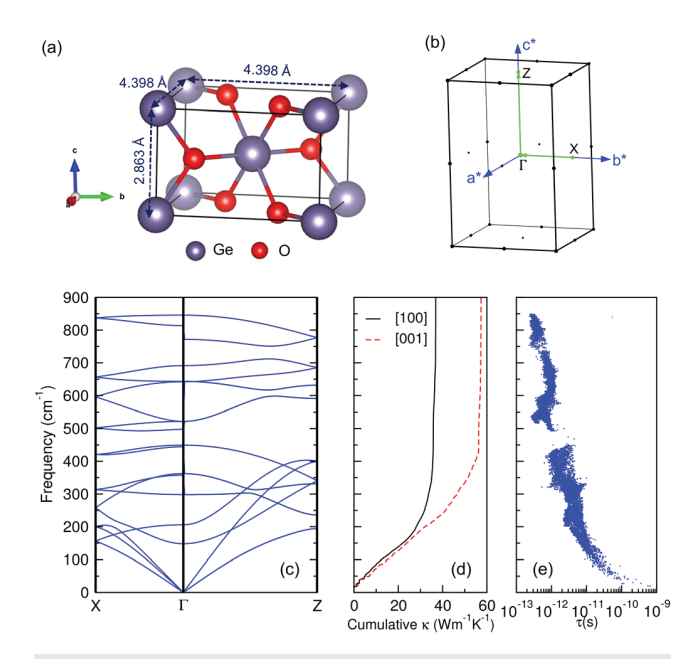


FIG. 1. (a) and (b) (a) Atomic structure and (b) Brillouin zone of rutile GeO $_2$ (c) phonon dispersion of r-GeO $_2$, including polar LO-TO splitting; (d) cumulative thermal conductivity at 300 K along the $\bot\vec{c}$ and $\parallel\vec{c}$ directions. The bulk thermal conductivity at 300 K is 37 W m $^{-1}$ K $^{-1}$ $\bot\vec{c}$ and 58 W m $^{-1}$ K $^{-1}$ $\parallel\vec{c}$. The accoustic modes have the largest contribution to thermal conductivity along both crystallographic directions. (e) Phonon lifetime due to three-phonon scattering as a function of phonon frequency. The lifetimes are the longest for the acoustic modes and show an overall decrease with increasing phonon frequency.

phonon-limited thermal conductivity is anisotropic, with values of $37~W~m^{-1}~K^{-1}~\bot\vec{c}$ and $58~W~m^{-1}~K^{-1}~\parallel\vec{c}$ at 300 K, reflecting the anisotropy of the rutile crystal structure. We find a directionally averaged thermal conductivity at 300 K of $44~W~m^{-1}~K^{-1}$ (theory) and $51~W~m^{-1}~K^{-1}$ (experiment), indicating that r-GeO $_2$ is a superior thermal conductor to $\beta\text{-Ga}_2\text{O}_3$ (11 W m $^{-1}~K^{-1}~\parallel\vec{a}$ and 27 W m $^{-1}~K^{-1}~\parallel\vec{b}$) and can overcome the thermal-dissipation limitations of $\beta\text{-Ga}_2\text{O}_3\text{-based}$ devices.

Our calculations are based on the Boltzmann transport equation (BTE) as implemented in the almaBTE software.9 The second-order (harmonic) interatomic force constants (IFCs) and Born effective charges were calculated within Quantum ESPRESSO¹⁰ using density functional theory (DFT) and density functional perturbation theory under the local-density approximation (LDA). 11,12 To obtain accurate phonon frequencies, a Ge^{4+} pseudopotential with the 3d electrons in the valence was used. The plane wave cutoff energy of 140 Ry converges the total energy of the system to within 1 mRy/atom. We generated the crystal structure of r-GeO2 starting from the experimental lattice parameters (space group = P42/mnm, Ge site = 0, 0, 0 and O site = 0.3060, 0.3060, 0). The structure was relaxed until the total pressure in the unit cell was 0.01 kbar and forces on the atoms were less than $|5 \times 10^{-6}|$ Ry/a₀. The relaxed parameters $a = 4.3736 \,\text{Å}$ and $c = 2.8674 \,\text{Å}$ differ from experiment ($a = 4.4066 \,\text{Å}$ and $c = 2.8619 \,\text{Å})^{13}$ by only 0.7% and 0.2%, respectively. The phonon frequencies were calculated on a $6 \times 6 \times 9$ Brillouin zone (BZ) [Fig. 1(b)] sampling grid, thus producing second-order IFCs on the same

supercell size. The third-order (anharmonic) IFCs were calculated using finite displacements on a $4\times4\times4$ supercell by manually shifting selected atoms and calculating the produced forces on surrounding atoms. A 0.5 nm nearest-neighbor distance cutoff was applied. The calculated relaxed structure, IFCs, and Born effective charges were applied within the almaBTE software, where an $18\times18\times27$ BZ sampling grid was used to calculate the thermal conductivity of r-GeO2 with the full BTE.

To synthesize bulk pellets of rutile-GeO₂, quartz-phase GeO₂ powders (Alfa Aesar, 99.999%) were loaded into a 10 mm-diameter graphite die and hot pressed at 800 °C under a pressure of 100 MPa for 3 h. The heating and cooling rate was 220 °C/h, and the pressing chamber was kept under vacuum (10⁻²Torr) throughout the process. X-ray diffraction (Rigaku Smartlab diffractometer equipped with a 1.54 Å Cu K α source) and scanning electron microscopy (JEOL IT500 SEM) were used to characterize the crystal structure and microstructure of our samples. The specific heat capacity and thermal diffusivity of r-GeO₂ pellets were measured on a laser flash system (Linseis LFA-1000) from room temperature to 677 K. Pellets were lightly coated with graphite spray, and the measurement was performed under flowing N2 gas. For each measurement step, we measured a Pyroceram 9606 reference sample and determined the measurement error, which is < 1% for specific heat capacity and < 4% for thermal diffusivity. The mass density was measured using Helium gas pycnometry on a Micromeritics Accupyc II 1340.

The calculated phonon dispersion of r-GeO2 is shown in Fig. 1(c). Longitudinal optical-transverse optical (LO-TO) splitting at Γ is observed for the four infrared (IR) active modes, with three of the modes splitting along the Γ —X direction and one along Γ —Z. The Born effective charges are +4.45 for Ge and -2.23 for O. The sound velocities of r-GeO₂ were reported previously $(4.67-9.44 \text{ km/s})^7$ and are higher than those of both GaN (3.69-7.67 km/s) and β -Ga₂O₃ (2.90–7.55 km/s). The LA modes along the Γ —Z direction extend up to a frequency of 400 cm⁻¹ that is approximately twice as large as that along Γ —X (205 cm⁻¹). This is due to the combination of a 1.4 higher LA sound velocity along Γ —Z (9.44 km/s) than along Γ —X (6.74 km/s)⁷ and the 1.5 times larger dimensions of the first BZ of r-GeO₂ along Γ —Z. At the edge of the BZ along Γ —Z, the frequency of the longitudinal-acoustic (LA) mode surpasses those of six optical modes, which indicates that simultaneous thermal activation of acoustic and optical modes can occur.

Figure 1(d) shows the thermal conductivity at 300 K and its cumulative distribution as a function of phonon frequency. The thermal conductivity at 300 K is 37 W m⁻¹ K⁻¹ $\perp \vec{c}$ and 58 W m⁻¹ K⁻¹ $\parallel \vec{c}$, resulting in a directional average of 44 W m⁻¹ K⁻¹. While several optical modes are mixed with the acoustic modes near the zone edges, a significant portion of the cumulative thermal conductivity is reached at the maximum acoustic-phonon frequencies. Along the $\perp \vec{c}$ direction, 77% of the total thermal conductivity is reached at the frequency of 205 cm⁻¹. The percentage is even higher for the $\parallel \vec{c}$ direction, with 95% of the total thermal conductivity reached at 400 cm⁻¹. Therefore, acoustic modes are the primary phonon modes responsible for heat conduction in r-GeO₂. Since the characteristic frequencies for the saturation of the cumulative thermalconductivity distribution coincide with the highest LA mode frequencies along the two main crystallographic directions, we conclude that the LA modes are likely the dominant modes that contribute to the thermal conductivity. Moreover, the ratio of the

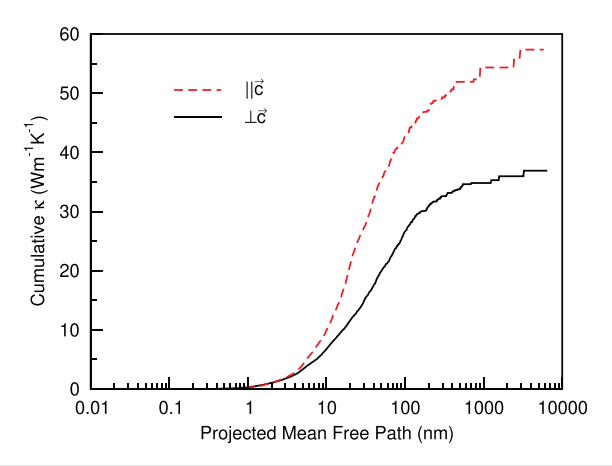


FIG. 2. Cumulative thermal-conductivity distribution of r-GeO $_2$ at 300 K as a function of the phonon mean free path. 90% of the maximum thermal conductivity along both directions is reached for a mean free path of 0.4 μ m.

thermal conductivity along the two axes ($\kappa_{\parallel c}/\kappa_{\perp c}=1.54$) is similar to the ratio of the corresponding LA sound velocities ($\nu_{\text{LA},\parallel c}/\nu_{\text{LA},\perp c}=1.4$), further indicating that the LA modes dominate thermal transport in r-GeO₂. The phonon lifetimes due to three-phonon scattering are plotted as a function of phonon frequency in Fig. 1(e). The lifetimes are the longest for the acoustic modes and show an overall decrease with increasing phonon frequency.

The dependence of κ on the phonon mean free path (MFP) proves to be useful to understand the thermal conductivity of polycrystalline samples and thin films, for which the MFP is determined by the grain size and film thickness, respectively. Figure 2 shows the cumulative thermal-conductivity distribution at 300 K along the $\perp \vec{c}$ and $\parallel \vec{c}$ directions as a function of phonon MFP. Along both directions, 90% of the maximum κ is reached at a phonon MFP of 0.4 μ m.

Figure 3 shows the x-ray diffraction (XRD) pattern and scanning electron microscopy (SEM) images for (a) and (b) quartz-GeO₂

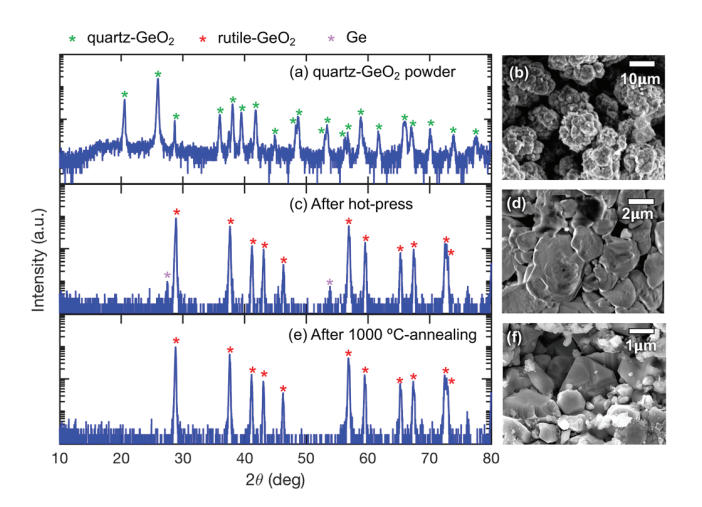


FIG. 3. X-ray diffraction pattern and scanning electron microscope images of (a) and (b) ${\rm GeO_2}$ powder, (c) and (d) a ${\rm GeO_2}$ pellet after hot pressing at 800 °C and 100 MPa, and (e) and (f) a ${\rm GeO_2}$ pellet after hot pressing (800 °C, 100 MPa) and subsequent annealing (1000 °C, air). A phase-pure rutile ${\rm GeO_2}$ pellet is obtained through hot-pressing and subsequent annealing, with grain sizes of 1.50 \pm 0.30 μ m.

powder and (c) and (d) the initial hot-pressed pellet, showing nearly 100% phase conversion to r-GeO2 after hot-press. However, we observe < 2% impurity Ge phase after hot pressing. In order to oxidize the Ge impurity phase, we annealed the hot-pressed pellet at 1000 °C in air [Figs. 3(e) and 3(f)]. Our XRD analysis shows that the final product is a single-phase, polycrystalline rutile GeO2 pellet with a grain size of 1.50 \pm 0.30 μm . We, therefore, conclude that the measured thermal conductivity of our polycrystalline sample is close to the intrinsic phonon-limited bulk value. We also measured a mass-density (ρ) value of 6.39 \pm 0.04 g/cm³ for the final product, which is 1.9% higher than the ideal value for rutile GeO2 (6.27 g/cm³).

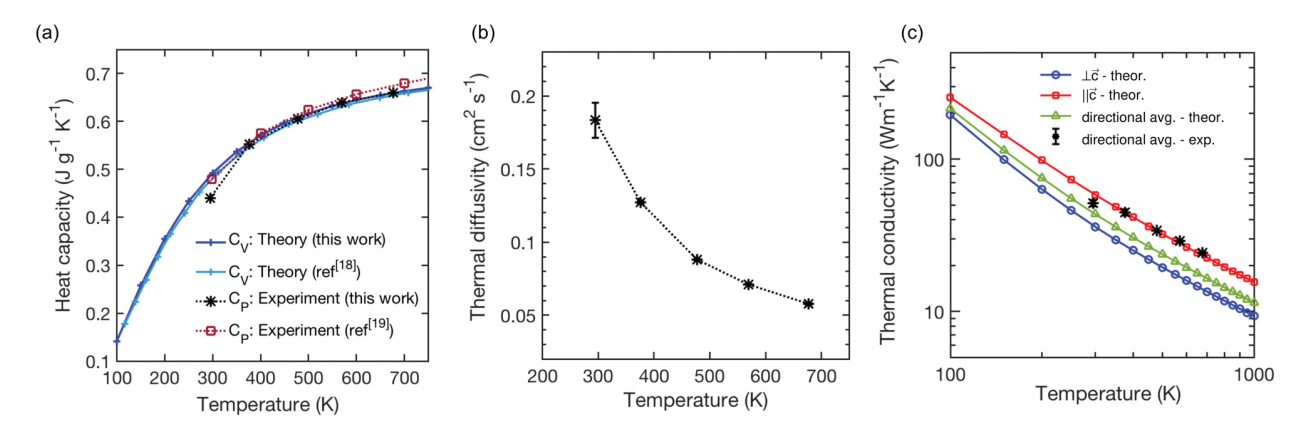


FIG. 4. (a) The calculated constant-volume specific heat (C_V) of r-GeO₂ and the measured constant-pressure specific heat (C_P) of r-GeO₂ as a function of temperature are in good agreement with each other and with previous work. ^{18,19} (b) Thermal diffusivity of polycrystalline r-GeO₂ measured as a function of temperature by the laser-flash method. (c) Experimental and theoretical thermal conductivity of r-GeO₂ from 100 K to 1000 K on the logarithmic scale. The theoretical values were calculated along both crystallographic directions and averaged according to $\kappa_{\text{avg}} = \frac{2}{3}\kappa_{\text{a}} + \frac{1}{3}\kappa_{\text{c}}$. Experimental measurements were performed on a polycrystalline r-GeO₂ sample with an average grain size of 1.50 \pm 0.30 μ m. The measured values are slightly higher than the directionally averaged theoretical values, but a consistent temperature dependency trend is observed between the theoretical and the experimental results.

Figures 4(a) and 4(b) show the specific heat capacity (C_p) and the thermal diffusivity (α) of r-GeO₂ as a function of temperature. The experimental constant-pressure specific heat is in good agreement with the calculated constant-volume specific heat capacity (C_V) since the difference between the two quantities $C_P - C_V = \frac{T\cdot V\cdot x^2}{K}$ is estimated to be less than 1% at room temperature, where V is the molar volume $(1.597 \times 10^{-7} \text{ m}^3/\text{g})$, α is the thermal-expansion coefficient $(14.2 \times 10^{-6} \text{ K}^{-1})$, and K is the compressibility $(4.05 \times 10^{-12} \text{ Pa}^{-1})$. The thermal conductivity $(\kappa = \alpha \cdot C_p \cdot \rho)$ is plotted as a function of temperature in Fig. 4(c) and compared with our calculated results. We observed that the measured thermal conductivity is slightly higher than the directionally averaged calculated values. We also observed the temperature dependence of the measured thermal conductivity to be consistent with the trend predicted by theory.

The thermal conductivity is one of the most important criteria to determine the performance of UWBG materials in power applications. $\beta\text{-}Ga_2O_3$ is one of the most promising materials for devices due to the high breakdown field; however, it suffers from poor thermal conduction due to the low symmetry of the monoclinic crystal structure. Our results demonstrate r-GeO_2 as an alternative UWBG material with superior thermal properties. The measured thermal conductivity of r-GeO_2 at 300 K (51 W m^{-1} K^{-1}) is approximately 2 times higher than the highest value of $\beta\text{-}Ga_2O_3$. Also, while $\beta\text{-}Ga_2O_3$ can only be grown on thermally poor substrates (e.g., Al_2O_3), the higher symmetry of r-GeO_2 may enable electronic device architectures with better thermal conduction. The higher thermal conductivity of r-GeO_2, along with its predicted ambipolar dopability and higher BFOM compared to $\beta\text{-}Ga_2O_3$, accentuates its potential for UWBG electronic applications.

In conclusion, we report the results of first-principles calculations and experimental measurements for the thermal conductivity of r-GeO $_2$ as a function of temperature. Our calculations predict phonon-limited thermal conductivities of $37\,\mathrm{W\,m^{-1}\,K^{-1}} \perp \vec{c}$ and $58\,\mathrm{W\,m^{-1}\,K^{-1}} \parallel \vec{c}$ at $300\,\mathrm{K}$. The measured thermal conductivity of our synthesized polycrystalline r-GeO $_2$ pellets with grain sizes of $1.50\pm0.30\,\mu\mathrm{m}$ at room temperature is $51\,\mathrm{W\,m^{-1}\,K^{-1}}$. From theory, we show that thermal transport occurs primarily through phonons with mean free paths shorter than $0.4\,\mu\mathrm{m}$, indicating that our experimental measurements are in the range of the single-crystal values. Our theoretical and experimental thermal conductivity results showcase that r-GeO $_2$ is a promising UWBG material with superior thermal conductivity to $\beta\text{-Ga}_2\mathrm{O}_3$ for efficient heat management in power-electronics applications.

AUTHORS' CONTRIBUTIONS

S.C. and K.A.M. contributed equally to this work.

We thank Jesús Carrete for useful discussions of thermalconductivity calculations. This work was supported as part of the Computational Materials Sciences Program funded by the U.S. Department of Energy, Office of Science, Basic Energy Sciences, under Award No. DE-SC0020129 (phonon and thermal-transport calculations), by the National Science Foundation Award No. DMR 1810119 (synthesis and structural characterization), and by the U.S. Department of Energy, Office of Science, Basic Energy Sciences under Award No. DE-SC00018941 (thermal transport measurements). It used resources of the National Energy Research Scientific Computing (NERSC) Center, a DOE Office of Science User Facility supported under Contract No. DE-AC02–05CH11231. K.A.M. acknowledges the support from the National Science Foundation Graduate Research Fellowship Program through Grant No. DGE 1256260.

DATA AVAILABILITY

The data that support the findings of this study are available from the corresponding author upon reasonable request.

REFERENCES

¹J. Y. Tsao, S. Chowdhury, M. A. Hollis, D. Jena, N. M. Johnson, K. A. Jones, R. J. Kaplar, S. Rajan, C. G. Van de Walle, E. Bellotti, C. L. Chua, R. Collazo, M. E. Coltrin, J. A. Cooper, K. R. Evans, S. Graham, T. A. Grotjohn, E. R. Heller, M. Higashiwaki, M. S. Islam, P. W. Juodawlkis, M. A. Khan, A. D. Koehler, J. H. Leach, U. K. Mishra, R. J. Nemanich, R. C. N. Pilawa-Podgurski, J. B. Shealy, Z. Sitar, M. J. Tadjer, A. F. Witulski, M. Wraback, and J. A. Simmons, Adv. Electron. Mater. 4, 1600501 (2018).

²Z. Guo, A. Verma, X. Wu, F. Sun, A. Hickman, T. Masui, A. Kuramata, M. Higashiwaki, D. Jena, and T. Luo, Appl. Phys. Lett. 106, 111909 (2015).

³L. Boteler, A. Lelis, M. Berman, and M. Fish, in IEEE 7th Workshop on Wide Bandgap Power Devices Applications (2019), p. 265.

⁴M. Stapelbroek and B. D. Evans, Solid State Commun. 25, 959 (1978).

⁵K. A. Mengle, S. Chae, and E. Kioupakis, J. Appl. Phys. **126**, 085703 (2019).

⁶S. Chae, J. Lee, K. A. Mengle, J. T. Heron, and E. Kioupakis, Appl. Phys. Lett. 114(5), 102104 (2019).

K. A. Mengle and E. Kioupakis, arXiv:1911.09750 (n.d.).

⁸P. Türkes, C. Pluntke, and R. Helbig, J. Phys. C **13**, 4941 (1980).

⁹J. Carrete, B. Vermeersch, A. Katre, A. van Roekeghem, T. Wang, G. K. H. Madsen, and N. Mingo, Comput. Phys. Commun. 220, 351 (2017).

10 P. Giannozzi, S. Baroni, N. Bonini, M. Calandra, R. Car, C. Cavazzoni, D. Ceresoli, G. L. Chiarotti, M. Cococcioni, I. Dabo, A. D. Corso, S. De Gironcoli, U. Gerstmann, C. Gougoussis, A. Kokalj, M. Lazzeri, L. Martin-samos, N. Marzari, F. Mauri, R. Mazzarello, S. Paolini, A. Pasquarello, L. Paulatto, and C. Sbraccia, J. Phys.: Condens. Matter 21, 395502 (2009).

¹¹D. M. Ceperley and B. J. Alder, Phys. Rev. Lett. **45**, 566 (1980).

¹²J. P. Perdew and A. Zunger, Phys. Rev. B **23**, 5048 (1981).

¹³ A. A. Bolzan, C. Fong, B. J. Kennedy, and C. J. Howard, Acta Crystallogr., Sect. B 53, 373 (1997).

¹⁴K. Sarasamak, S. Limpijumnong, and W. R. L. Lambrecht, Phys. Rev. B 82, 035201 (2010).

15K. A. Mengle and E. Kioupakis, AIP Adv. 9, 015313 (2019).

¹⁶K. V. K. Rao, S. V. N. Naidu, and L. Iyengar, J. Appl. Crystallogr. 6, 136 (1973).

¹⁷V. B. Prakapenka, L. S. Dubrovinsky, G. Shen, M. L. Rivers, S. R. Sutton, V. Dmitriev, H. P. Weber, and T. Le Bihan, Phys. Rev. B 67, 132101 (2003).

¹⁸P. Hermet, A. Lignie, G. Fraysse, P. Armand, and P. Papet, Phys. Chem. Chem. Phys. 15, 15943 (2013).

¹⁹R. J. L. Andon and K. C. Mills, J. Chem. Thermodyn. **3**, 583 (1971).